Clinical radiation dose verification by topographic persistent luminescence dosimetry

Zichao Luo [a,1], Yayun Wu [b,1], Yuenan Wang [c], Dehong Hu [b], Duyang Gao [b], Yongshuai Ge [b], Zonghai Sheng [b,*], Xiaogang Liu [a,d,**], Hairong Zheng [b,*]

[a] Department of Chemistry and the N.1 Institute for Health, National University of Singapore, 117543, Singapore
[b] Paul C. Lauterbur Research Center for Biomedical Imaging, Institute of Biomedical and Health Engineering, Shenzhen Institute of Advanced Technology, Chinese Academy of Sciences, Shenzhen 518055, PR China
[c] Department of Radiation Oncology, Peking University Shenzhen Hospital, Shenzhen 518036, PR China
[d] Institute of Materials Research and Engineering, Agency for Science, Technology and Research, 138634, Singapore

ARTICLE INFO

ABSTRACT

Radiation dose verification in radiotherapy is essential to determine the dose delivered to irradiated tissue while minimizing normal tissue toxicity. However, the challenge remains in determining topographic radiation dose profiles due to limitations in conventional dosimeters. Herein, we report a robust technique for visualizing and verifying clinical doses based on reusable, flexible scintillating films comprising lanthanide-doped persistent luminescent nanoparticles. These nanoparticle-based films outperform commercially available radiochromic films in terms of linear response to irradiation doses between 0 and 25 Gy. We demonstrate topographic persistent luminescence dosimetry for radiotherapy of mice and rabbits with malignant tumors. Our data show a higher signal-to-background ratio, especially at lower (< 0.1 Gy) and higher (> 10 Gy) X-ray doses. We also demonstrate that topographic persistent luminescence dosimetry can record complex clinical dose distributions for dose verification and radiotherapy planning.

© 2023 Published by Elsevier Ltd.

Introduction

Radiotherapy is an important and widely used cancer treatment that uses ionizing radiation to kill tumor cells [1]. Radiotherapy is used in approximately 60% of cancer patients for both curative and palliative purposes and can also be used in conjunction with any other cancer treatment [2]. To date, modern and precision radiotherapies, such as intensity-modulated radiotherapy, image-guided radiotherapy, and dose-guided radiotherapy, have greatly increased patient survival, owing to great improvements in computer-aided and high-precision treatment planning [3,4]. Despite these achievements, modern radiotherapy still causes side effects, including acute gastrointestinal erythema, desquamation, and necrosis, which are associated with over-irradiation and inaccurate X-ray doses [5,6].

The radiotherapy workflow includes tumor segmentation, treatment planning, quality assurance (dose verification), and delivery [7]. Precise and rigorous quality assurance is critical to improving the therapeutic index [8,9], because it ensures precise dose delivery to the tumor. Clinical dosimeters based on thermoluminescence, ionization chambers, and silicon diodes give accurate X-ray point-dose measurements [10]. However, they cannot map topographic dose profiles and identify overexposed regions [10,11]. They are also time-consuming to operate and necessitate the services of a radiology technician [12,13]. To overcome these limitations, X-ray responsive radiographic or Gafchromic films (HD-810, EBT, EBT2, and EBT3) have been used to verify topographic doses [14,15]. However, their clinical application is hindered by long waiting times, high costs, and relatively narrow detection ranges [15,16]. The response of these dosimeters is also affected by operating conditions (e.g., humidity, pressure, and temperature) [14,17].

Molecular and nanosystem-based dosimeters, including organic and inorganic molecules, quantum dots, polymers, plasmonic nanoparticles, carbon nanotubes, and metal-organic frameworks, have been used to determine X-ray doses in radiotherapy [12,18–31]. Despite advancements, these dosimeters have difficulties, such as

---

* Corresponding authors.
** Corresponding author at: Department of Chemistry and the N.1 Institute for Health, National University of Singapore, 117543, Singapore.
E-mail addresses: zh.sheng@siat.ac.cn (Z. Sheng), chmlx@nus.edu.sg (X. Liu), hr.zheng@siat.ac.cn (H. Zheng).
[1] Zichao Luo and Yayun Wu contributed equally to this work.
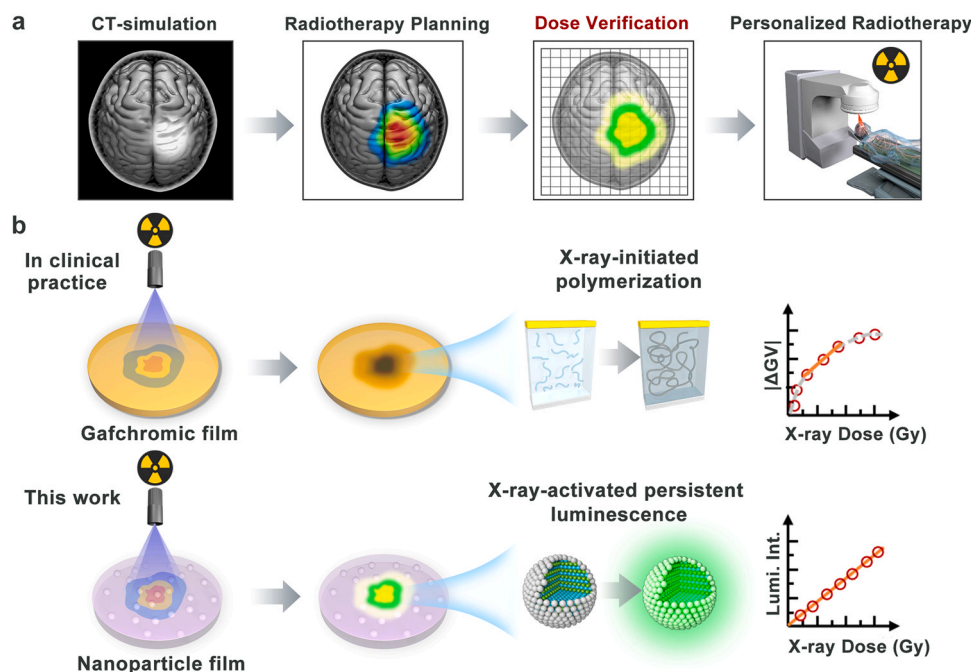
Fig. 1. Topographic persistent luminescence dosimetry for clinical dose verification and visualization. (a) The main workflow of tumor radiotherapy in the clinic. (b) Comparative analysis of the working mechanisms of Gafchromic film and the persistent luminescent nanoparticle film for clinical dose verification.

measuring point doses, low stability, low sensitivity, or long waiting times after irradiation. Herein, we present a dosimetry technique based on lanthanide-doped nanoparticle films for topographic persistent luminescence dosimetry (Fig. 1). After X-ray irradiation, the persistent luminescence signal of the film measures ionizing radiation. The nanoparticle film permits rapid X-ray dose determination and topographic radiation dose mapping in mouse and rabbit models. We further demonstrate its utility for radiation planning in clinical cancer radiotherapy. Our results imply that the nanoparticle film has great promise for topographic dose determination during radiation treatment.

Materials and methods

Materials

Acetate hydrate lutetium(III) (Lu(CH_3CO_2)$_3$•xH_2O, 99.9%), acetate hydrate terbium (III) (Tb(CH_3CO_2)$_3$•xH_2O, 99.9%), sodium hydroxide (NaOH, > 98%), ammonium fluoride (NH_4F, > 98%), 1-octadecene (ODE, 90%) and oleic acid (OA, 90%) were purchased from Sigma-Aldrich. Methanol anhydrous (AR, ≥99.5%), ethanol anhydrous (AR, ≥99.7%), dichloromethane (AR, ≥99.5%), and cyclohexane (AR, ≥99.7%) were purchased from Sinopharm Chemical Reagent Co., Ltd. (Shanghai, China). SYLGARD™ 184 silicone elastomer kit was purchased from Dow Corning. Round quartz glass plates were purchased from Square Optics (Lianyungang, China). The lead sheet (size: 0.8 mm × 55 mm×150 mm) was purchased from Yule Forefront Co., Ltd. (Shenzhen, China). Gafchromic™ RTQA2–1010 film was purchased from Ashland.

Synthesis of NaLuF$_4$:Tb nanocrystals

Oleic acid-capped NaLuF$_4$:Tb (Tb=15%, mol%) nanocrystals were synthesized by a co-precipitation method. Briefly, a mixture of Lu (CH_3CO_2)$_3$•xH_2O (0.85 mmol) and Tb(CH_3CO_2)$_3$•xH_2O (0.15 mmol) was added into a 50-mL three-necked round-bottom flask containing 10 mL of OA and 15 mL of ODE. The mixture was degassed in a vacuum and heated to 150 °C for 30 min. After cooling to room temperature, 20 mL of methanol containing 4 mmol NH_4F and 2.5 mmol NaOH were added to the mixture and stirred at 50 °C for 30 min. Then the mixture was heated to 100 °C under vacuum for 30 min to remove residual methanol, and then quickly heated to 300 °C for 1.5 h under a nitrogen atmosphere with stirring. After cooling to room temperature, as-synthesized core nanocrystals were precipitated with excess ethanol, collected by centrifugation at 6000 rpm for 5 min, washed twice with ethanol, then dispersed in 8 mL of cyclohexane and stored in a freezer at 4 °C for further use.

Fabrication of the scintillating film

The as-prepared lanthanide-doped nanoparticles (NaLuF$_4$:Tb) were precipitated with excess ethanol and re-dispersed in dichloromethane at a concentration of 10 mg mL^{-1}. The SYLGARD™ 184 silicone elastomer base was mixed with the curing agent (10:1, mass ratio). Then, 10 mL of nanocrystals were added into 10 mL of the above elastomer base solution under vigorous stirring. The resultant solution was then degassed under vacuum to remove organic solvents and air bubbles.

Round quartz glass plates were pretreated with a gas plasma dry cleaner for 5 min. To prepare a scintillating film, the mixture solution was spin-coated on the round quartz glass substrate at 600 rpm for 60 s and then dried at 120 °C for 10 min. After cooling to room temperature, the as-prepared scintillating film was stored in a dark place for further use. Scintillating films prepared at different rotational speeds (800, 1000, 2000, 3000 rpm) or nanoparticle dopants (0.8%, 0.6%, 0.4%, 0.2%, w/v) were prepared by the same procedure.

Physical characterization

Transmission electron microscopy and high-resolution transmission electron microscopy (HRTEM) images were taken using a Tecnai G2 F30 microscope (FEI, USA) and operated at an accelerating voltage of 200 kV. Radioluminescence spectra were acquired using an Edinburgh FS5 fluorescence spectrophotometer (Edinburgh Instruments Ltd., U.K.) equipped with a miniature X-ray source (Amptek, Inc., USA). Scanning electron microscopy images were

acquired with a SU 3500 Hitachi scanning electron microscope. XRD patterns were obtained using an X-ray powder diffractometer (D8 Advance, Bruker, Germany) over an angular range of 5–90°. Atomic force microscopy images were obtained using a Park XE7 (Park Systems, Korea). The height of the scintillation films was characterized using a Zeta-20 optical profiler (KLA, USA).

X-ray-activated persistent luminescence imaging of scintillating films

An X-ray source from RS2000 pro biological X-ray irradiator (Rad Source Technologies, USA) or a medical CT light source (Varex G-242, Varex Imaging Corporation, USA) was applied to activate scintillating films. After a 2-min X-ray exposure, luminescence images were recorded using an IVIS Lumia II in vivo imaging system (Perkin Elmer, USA) in a high-sensitivity bioluminescence imaging mode. Luminescence images were acquired at different time points after X-ray irradiation. Mean luminescence intensity was measured using Image J software and normalized according to I_n (normalized luminescence intensity) $= I_{lumi}$ (mean luminescence intensity)$/t_{exp}$ (exposure time). All luminescence intensities used for the calculation are the normalized luminescence intensity in this study. The I_n decay curves are fitted to a bi-exponential decay function [32,33]:

$$I_n(t) = I_0 + A_1 \exp\left(-\frac{t}{\tau_1}\right) + A_2 \exp\left(-\frac{t}{\tau_2}\right)$$

Where I_n and I_0 are the luminescence intensities; A_1 and A_2 are constants; t is the time after cessation of X-ray; τ_1 and τ_2 are the decay times of exponential components. The function of the relationship between the luminescence intensity, the time after cessation of X-rays, and the radiation dose is shown in Fig. S6 online.

To study the uniformity of the persistent luminescence intensity of the nanoparticle film, a matrix (5 ×5 grid) was randomly placed onto the image of the nanoparticle film as a region of interest (ROI). Then, the mean fluorescence intensity (I_m) of the whole matrix was measured using Image J software. Next, the mean fluorescence intensity of each small grid in the matrix was measured as I_s. The ratio of I_s/I_m was marked as the luminescence intensity in each small grid of the matrix. The heatmap of the luminescence intensity of each small grid in the matrix was produced according to ratios.

X-ray imaging of the phantom

Lead models with different shapes (triangle, square, circle or rhombus; length or diameter at 15 mm) were utilized for X-ray imaging of the phantom. The lead model was placed on the surface of the nanoparticle film and irradiated with X-rays (40 kV, 1 mA). Luminescence images were captured using an IVIS Lumia II in vivo imaging system 5 min after X-ray irradiation.

Scintillating films for X-ray-induced dynamic imaging after X-ray irradiation

The scintillating films were irradiated with 2 Gy X-rays, and luminescence images were acquired at different time points after X-ray irradiation (5, 8, 11, 14, 17, 20, 23, 26, 29, 32, 35, 38, 41, 44, 47, 50, 53, 56, 59, 62, 68, 74, 80, 86, 92, 102, 112, 122, 128, 138 min), and the average luminescence intensity was measured using Image J software. Then, the emission intensity was applied to calculate the dose delivered to the film according to the function in Fig. S6 online.

Comparison of standard curves for X-ray dose determination

Two types of films were designed for exposure to four different X-ray dose gradients (0/0.02/0.04/0.06/0.08/0.1 Gy, 0/0.1/0.2/0.3/0.4/ 0.5 Gy, 0/1/2/3/4/5 Gy, 0/5/10/15/20/25 Gy). First, two kinds of films

were irradiated with the designed X-ray dose within 2 min by adjusting the delivered X-ray dose rates. For the nanoparticle film, luminescence intensity was measured at 5 min after X-ray irradiation. For the Gafchromic film, images were captured with a digital camera (SONY, Japan) after X-ray irradiation, and the average gray values of red channels were measured using Image J software. Then, the linear fitting between the X-ray dose and the normalized luminescence intensity of the nanoparticle film or the average gray values of the Gafchromic film was conducted using Origin 2017.

Standard curves for determining the delivered X-ray dose during radiotherapy

Standard curves for X-ray dose determination based on nanoparticle or Gafchromic films were established under exposure to different X-ray doses (0–30 Gy). For a nanoparticle film, a linear standard curve was established between the normalized luminescence intensity and the delivered X-ray dose (0–30 Gy). For Gafchromic films, the gray values (GV) of red channels were transformed to the absolute values of decrements ($\Delta GV = |GV_0-GV|$, GV_0, gray value before irradiation; GV, the gray value after irradiation), since the gray values (GV) of red channels decreased with increase in X-ray dose. Then, the $\Delta GV|$ values of the Gafchromic film and the X-ray dose were fitted by the rational function according to a previous study [34]:

$$y = ax/(b + x)$$

Where a and b are constants; x is the X-ray dose; y is the $|\Delta GV=$ value.

Quantitative X-ray imaging of tumor radiotherapy in mice and rabbits

4T1 tumor-bearing Balb/c mice (tumor size: 1 cm × 1 cm; female, 20 g) were subjected to X-ray-induced radiotherapy. First, a nanoparticle film or a Gafchromic film was placed on tumor sites. Then, a lead plate with a square hole (1 cm × 1 cm) was placed over the film so that the tumor sites could be irradiated with X-rays. Subsequently, the tumor sites were irradiated with a serial of X-ray doses (0.06/1/5/10/20 Gy) for 2 min, and the films were recorded 5 min after cessation of X-rays.

For large tumor radiotherapy, VX2 tumor-bearing New Zealand white rabbits (female, 3 kg, tumor size: 2 cm × 5 cm) were used. After placing a nanoparticle or Gafchromic film on tumor sites, we placed a lead plate with an irregular hole (2 cm × 5 cm) over the film to protect other parts except the tumors from X-rays. Then, rabbits received X-ray-induced radiotherapy with different doses (0.1/1/10/ 20 Gy) within 2 min. Subsequently, the films were recorded 5 min after the end of irradiation according to the procedure described above.

The region of interest was randomly placed in a matrix (5 × 5 grids) and the average dose of each subset in the matrix was calculated according to standard curves (Fig. S9 online). In addition, the signal-to-background ratio was also calculated as I_{expose}/I_{shield} (I_{expose}, luminescence intensity in the X-ray exposed region; I_{shield}, luminescence intensity in the shielded region) for nanoparticle films or $|\Delta GV_{expose}|/|\Delta GV_{shield}|$ for Gafchromic film.

X-ray dose verification for clinical radiotherapy

Radiotherapy quality assurance (QA) plans for four patients were retrospectively selected for this study with approval from the local institution's internal review board (IRB). Four radiotherapy plans for four cancer patients who had received precision radiotherapy (TrueBeam™, Varian Medical Systems, USA) at Peking University Shenzhen Hospital (Shenzhen, China) were retrospectively applied to conduct dose verification for nanoparticle films. According to the
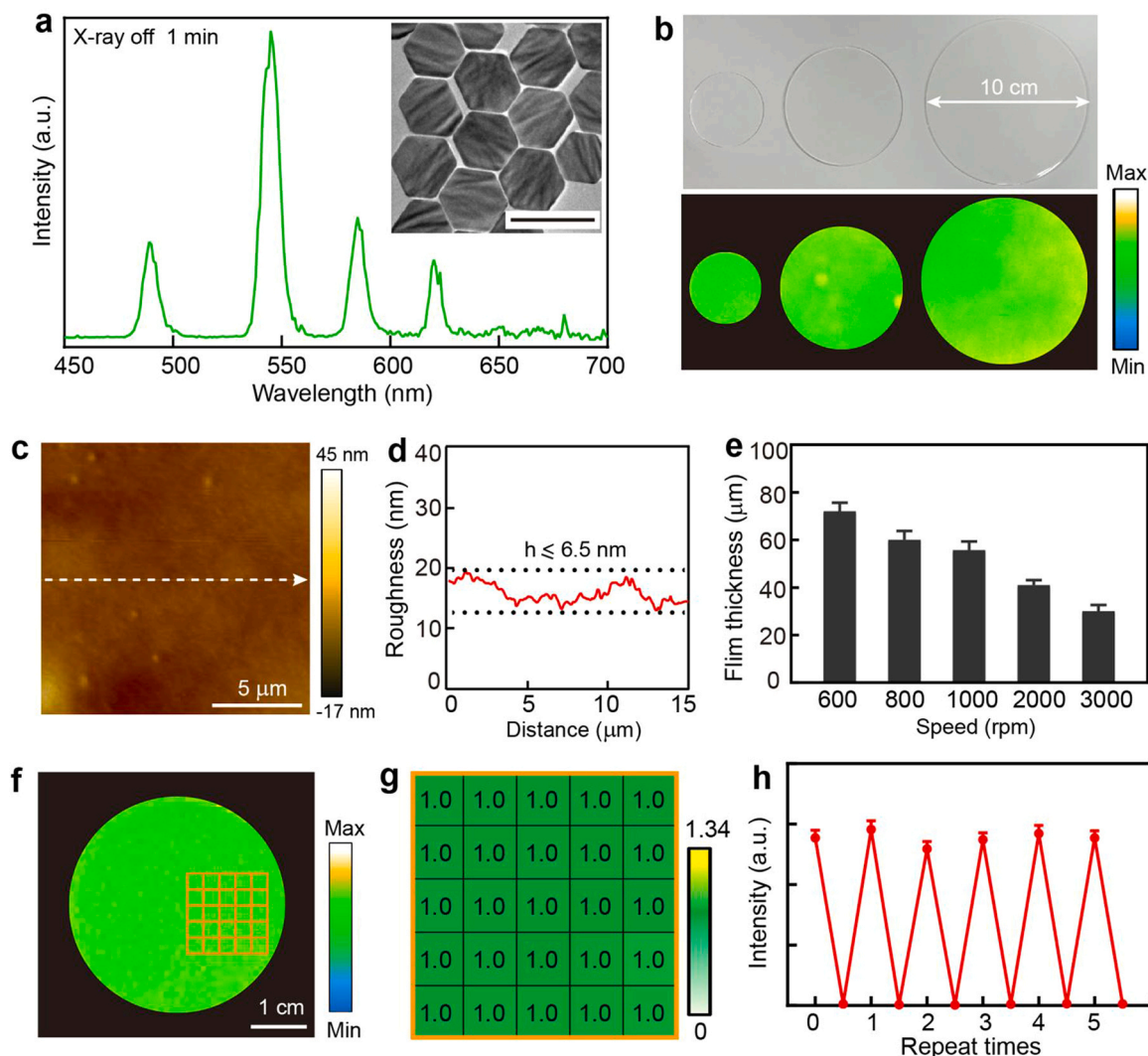
Fig. 2. Characterization of the nanoparticle film for luminescence dosimetry. (a) Persistent luminescence spectrum of as-synthesized NaLuF$_4$:Tb (15%) nanoparticles, recorded 1 min after cessation of X-rays (40 kV, 1 mA). The inset shows a typical TEM micrograph of the nanoparticles. Scale bar, 200 nm. (b) Photographs of nanoparticle films of different diameters before (top) and after X-ray irradiation (bottom). (c) Atomic force microscope image of the nanoparticle film. (d) Surface roughness of the nanoparticle film marked with a white dashed line in c. (e) Film thickness controlled by different spin-coating speeds. (f) Photograph of the nanoparticle film in response to X-rays. (g) Persistent luminescence intensity mapping in a random 5 × 5 grid marked in g. (h) Photostability of the nanoparticle film against repeat X-ray irradiation. Data are shown as mean ± s.e.m. (n = 3).

planning, nanoparticle films were topographically irradiated with different X-ray doses in a solid water phantom (Fig. S11 online). Luminescence images of the nanoparticle films were then captured, and radiation dose profiles were analyzed using standard curves, with clinical radiotherapy planning as a reference. The standard curves for luminescence intensity associated with X-ray dose were used as shown in Fig. S9 online. Clinical Gafchromic films were irradiated and used as controls.

Cell viability of 4T1, Raw 264.7 and bEnd.3 cells treated with verified X-ray doses

4T1, Raw 264.7, and bEnd.3 cells were seeded in different 96-well plates at a density of 7000 cells per well. After 24 h of incubation, cells were irradiated with different X-ray doses according to the radiotherapy planning (2, 4, 6, 8 Gy), the nanoparticle film-verified dose (which is 3.2% higher than the planning dose, 2.1, 4.1, 6.2, 8.3 Gy) or the Gafchromic film-verified dose (which is 18.5% higher than the planning dose, 2.4, 4.7, 7.1, 9.5 Gy). After another 24-h incubation, cell viability was analyzed using CCK-8 kits.

For live/dead staining, cells were first irradiated with an X-ray dose of 6.2/7.1 Gy or 8.3/9.5 Gy, then incubated at 37 °C for 24 h. Cells were stained with Calcein-AM/PI staining kits as described in the manual. Fluorescence images of cells were captured using a fluorescence microscope.

Results and discussion

Preparation of the lanthanide-doped nanoparticle film

We first prepared persistent luminescent terbium (Tb^{3+})-doped NaLuF$_4$ nanoparticles (NaLuF$_4$:Tb, Tb:15%) by a co-precipitation method [35]. After X-ray irradiation (40 kV, 1 mA), hexagonal nanoparticles with an average size of 130 nm emitted persistent luminescence in the range of 450–650 nm (Fig. 2a and S1 online), consistent with a previous study [35]. After embedding these nanocrystals in a polydimethylsiloxane (PDMS) membrane (1%, w/v), we spin-coated them to form a uniform film on a quartz substrate (Fig. S2 online). After heating and trimming, we obtained a series of smooth films with different diameters (5, 8, 10 cm) (Fig. 2b). The whole film showed a uniform persistent luminescence signal upon
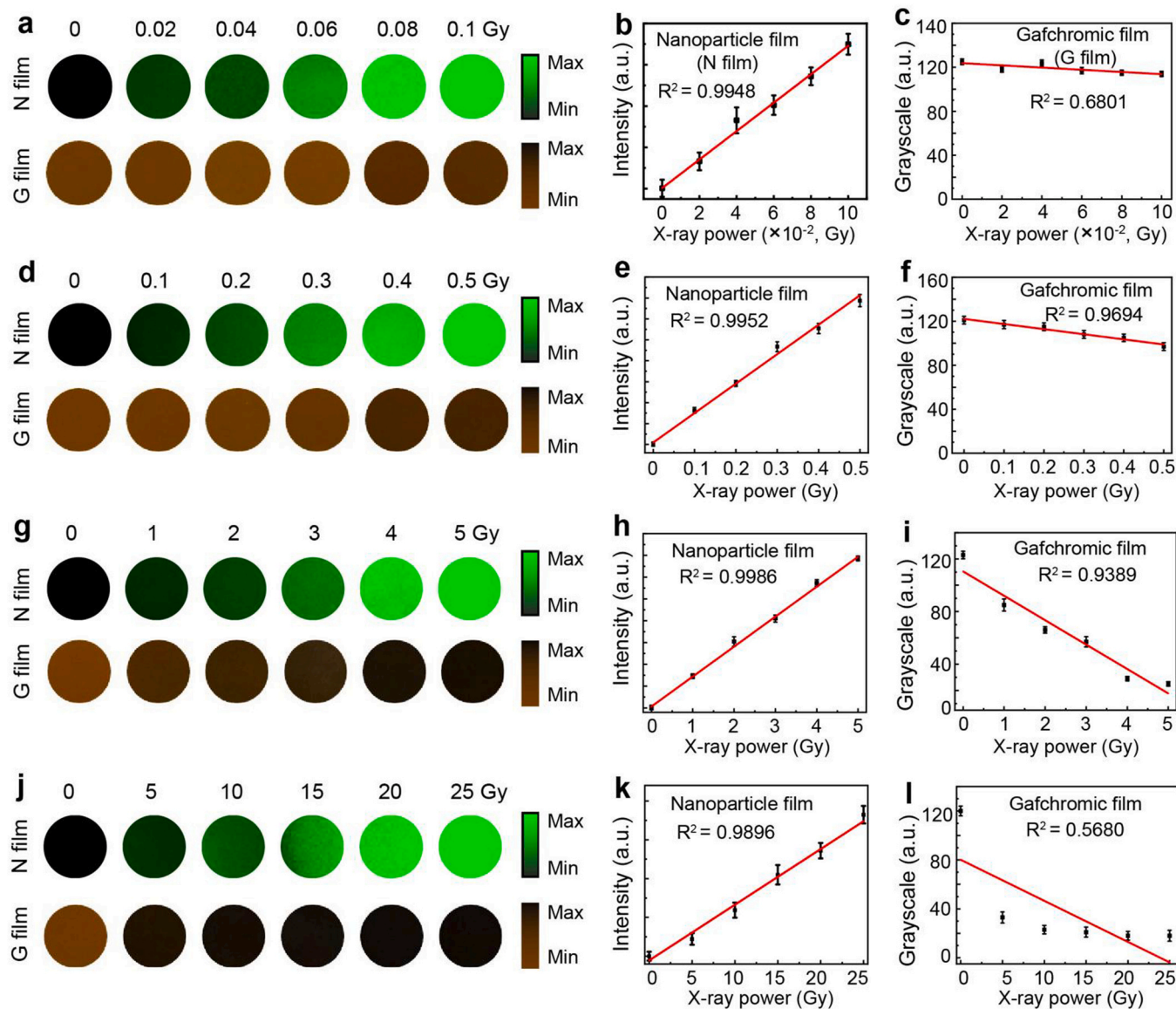
Fig. 3. Comparison of X-ray dose detection using nanoparticle and Gafchromic films. (a, d, g, j) Recorded photographs of nanoparticle and Gafchromic films after X-ray irradiation in the range of 0–0.1 Gy, 0–0.5 Gy, 0–5 Gy, and 0–25 Gy, respectively. b, c, Linear fitting of the luminescence intensity and the grayscale, respectively, versus X-ray dose for films shown in a. (e, f) Linear fitting of the luminescence intensity and grayscale, respectively, versus X-ray dose for films shown in d. (h, i) Linear fitting of the luminescence intensity and grayscale, respectively, versus X-ray dose for films shown in g. (k, l) Linear fitting of the luminescence intensity and grayscale, respectively, versus X-ray dose for films shown in j. Data are presented as mean ± s.e.m. (n = 3).

X-ray irradiation (40 kV, 1 mA) (Fig. 2b). Scanning electron micrograph of the film's transverse surface confirmed nanoparticle encapsulation into the film (Fig. S3 online). Atomic force microscopy showed that film roughness was less than 6.5 nm (Fig. 2c and d). We optimized the film by adjusting nanocrystal concentration and coating speed. The film thickness decreased from 72 to 30 μm when the spin-coating speed increased from 600 to 3000 rpm (Figs. 2e and S4 online). The luminescence intensity of the film decreased with increasing spin-coating speed and increased with increasing nanoparticle concentration (Fig. S4 online).

We selected the brightest film (1% w/v, 600 rpm) for further study. After X-ray exposure, a 5 × 5 randomly selected grid on the film emitted the same luminosity (Fig. 2 f and g). The film's homogeneity allows for reliable X-ray dose measurement. Importantly, similar luminescence intensity can be repeatedly excited with X-rays, which is not attainable by conventional X-ray films (Figs. 2h and S5 online). In addition, the scintillating film emitted uniform,

persistent luminescence even after 5 months of storage at room temperature (Fig. S5 online).

Nanoparticle film calibration curves versus X-ray dose

After irradiation, the luminescence intensity and X-ray dose were correlated quantitatively. Five scintillating films were irradiated with 1, 2, 3, 5, and 10 Gy, and emission intensities were measured within 2 h. Persistent luminescence increased with X-ray dose and decreased with time after irradiation (Fig. S6 online). In addition, the time factor post-irradiation can be fixed by uniformizing and assessing the emission intensity of standard and detection samples. Unless otherwise stated, we measured nanoparticle film luminescence 5 min post-irradiation.

Four dose ranges (0–0.1 Gy, 0–0.5 Gy, 0–10 Gy, or 0–25 Gy) were irradiated to Gafchromic or nanoparticle films, and then eight calibration curves were established based on luminescence intensity for
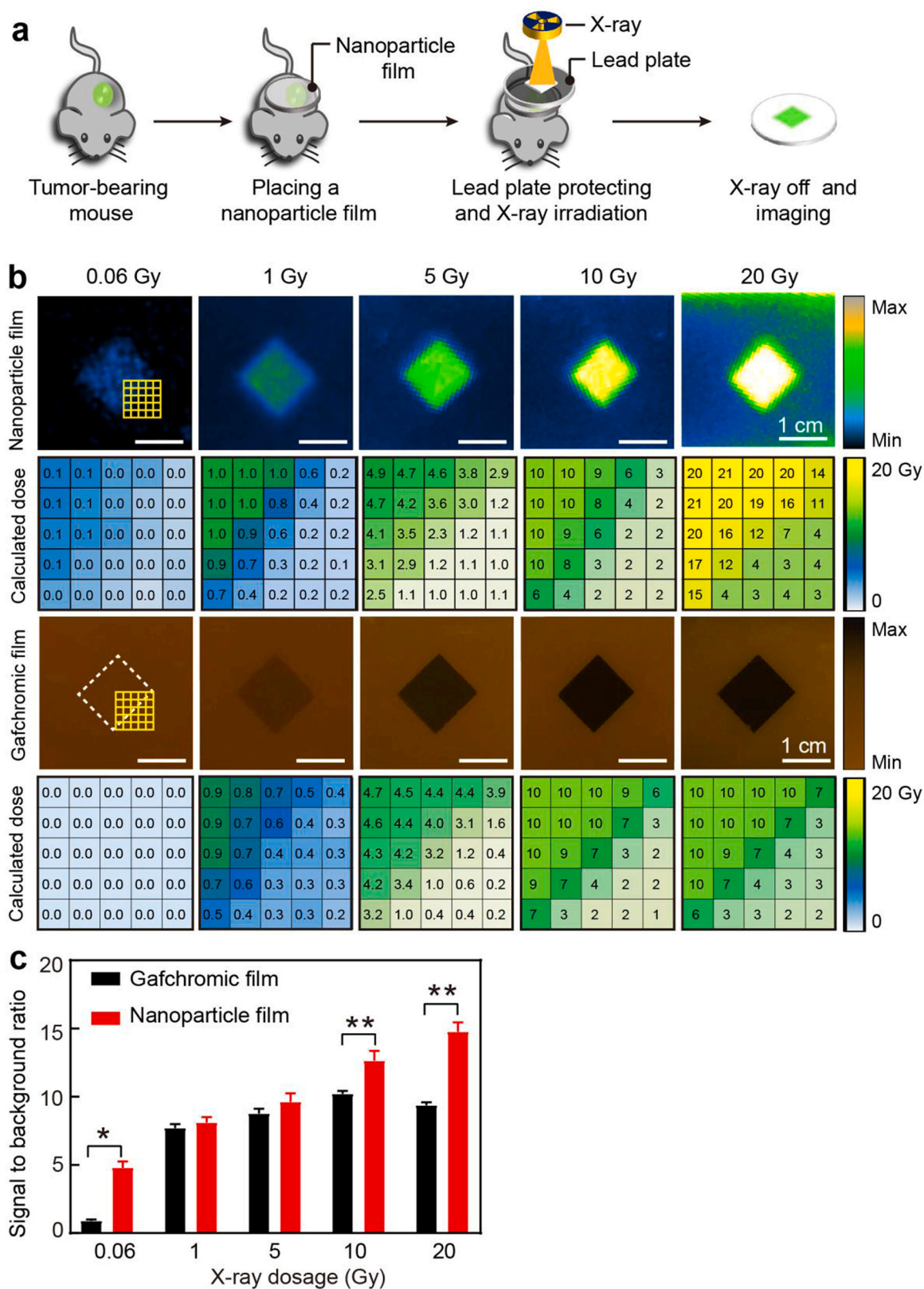
Fig. 4. Topographic persistent luminescence dosimetry for mouse tumor radiotherapy. (a) Schematic of X-ray dose detection for small tumor radiotherapy in mice. (b) Images of nanoparticle and Gafchromic films under X-ray irradiation with varied doses in a mouse tumor model, and the corresponding calculated "heat map" of the radiation dose delivered to the 5 × 5 grid. Blue and yellow colors in these grids represent lower and higher radiation doses, respectively. The grid value denotes the calculated X-ray dose based on the standard curves in the Supporting Materials and Methods. (c) Image signal-to-background ratios from nanoparticle and Gafchromic films in b. Data represent means ± s.e.m. (n = 3, $^*p < 0.05$; $^{**}p < 0.01$; student t-test.).

Fig. 5. Topographic persistent luminescence dosimetry for clinical radiotherapy of four different tumors. (a) Images of the nanoparticle and Gafchromic films used for dose verification. Tumor sites are highlighted in red in computed tomographic images. (b) Corresponding calculated "heat map" of the radiation dose delivered to the 8 × 8 grid from 4 patients in a (i, radiotherapy planning; ii, Gafchromic film; iii, nanoparticle film). Green and yellow colors in these grids represent lower and higher radiation doses, respectively. The grid value denotes the calculated X-ray dose based on the standard curves in the Supporting Materials and Methods.

Fig. 6. Cell viability of 4T1 tumor cells, Raw 264.7 cells, and bEnd3 cells treated with different X-ray dosages. (a-c) Investigation of 4T1 cells, Raw cells, and bEnd3 cells, respectively, under different X-ray doses according to the radiotherapy planning and dose verification from the nanoparticle film (3% higher than the planning dose) and Gafchromic film (15% higher than the planning dose). After incubation for 24 h, cell viability was measured using a CCK-8 kit. Cells without X-ray irradiation were used as a positive control. (d, e) Calcein-AM/PI staining analysis of three types of cells treated with verified X-ray doses derived from the nanoparticle film (6.2 and 8.3 Gy) or Gafchromic film (7.1 and 9.5 Gy). Calcein-AM, calcein acetoxymethyl ester. PI, propidium iodide. Scale bar, 200 μm. Data represent means ± s.e.m. (n = 6, ** $p < 0.01$; *** $p < 0.001$; ns, not significant; student *t*-test.).

the nanoparticle film or gray value for Gafchromic film. All standard curves were generated using linear fitting so that they could be easily compared. The color of the Gafchromic film does not change at 0–0.1 Gy, and the standard curve decreases nonlinearly ($R^2 = 0.6801$) (Fig. 3a and c). In contrast, nanoparticle films exhibit obvious color changes, and the ensuing treatment showed a substantial linear increase ($R^2 = 0.9948$) (Fig. 3a and b).

Gafchromic film darkened with increasing X-ray dose, and the response curves decreased linearly (0–0.5 Gy, $R^2 = 0.9694$; 0–5 Gy, $R^2 = 0.9389$). These results indicate that the Gafchromic film can determine radiation doses between 0 and 5 Gy (Fig. 3d-i), consistent with a previous report [36]. Good linear calibration curves show that scintillating films can detect the above two ranges, as evidenced (Fig. 3d-i). However, over 10 Gy, the Gafchromic film showed no color change and the calibration curve had a low R^2 value (0.5680) (Fig. 3j and l). In contrast, the nanoparticle film showed high sensitivity to high X-ray doses (> 10 Gy), as evidenced by a good linear fit between 0 and 25 Gy ($R^2 = 0.9896$) (Fig. 3j and k).

The nanoparticle film-based X-ray dosimeter can detect point doses and map radiation profiles. After X-ray irradiation (40 kV, 1 mA) of lead models (square, circle, triangle, or parallelogram), different shapes are obtained (Fig. S7 online). It is also possible to achieve X-ray imaging of two squares of different sizes based on nanoparticle films. Analysis of the random grid showed that each small grid had the same dose (Fig. S7 online).

Note that persistent luminescence emitted from lanthanide-doped nanoparticles gradually decreased with time post X-ray radiation. The nanoparticle film was then applied for dynamic imaging

of the X-ray dose in vitro. The luminescence signal of the film became weaker with increasing time after X-ray exposure, but the calculated dose of each small grid was almost the same because of the time factor (Figs. S6 and S8 online). This unique dynamic imaging and calculation capability is different from existing dosimeters, which is attributed to the unique optical property of X-ray-activated persistent luminescent nanocrystals.

Pre-clinical dose determination

We employed scintillating films to detect the X-ray dose to small tumors in mice (~1 cm × 1 cm). To deliver X-rays exclusively to tumor sites, a lead plate with a square hole (~1 cm × 1 cm) was placed on the films, covering the rest of the body of the mice except the tumors (Fig. 4a). X-ray responsive films were collected and examined after varied X-ray dosages. The luminous signal of the nanoparticle film grew with increasing radiation dose (0.06–20 Gy), while the Gafchromic film darkened with increasing radiation dose (0.1–10 Gy) (Fig. 4b). The nanoparticle film was more sensitive to the X-ray dose than the Gafchromic film, notably at low doses (< 0.1 Gy) or high doses (> 10 Gy).

Calibration curves were then used to calculate X-ray doses (Fig. S9). In all treatments, the calculated dose from the nanoparticle film matched the given dose in the irradiation zone (upper left corner of the 5 ×5 gird) (Fig. 4b). Moreover, the computed dose decreased toward the irradiation boundary (near the 5 ×5 gird diagonals), due to a decrease in delivered X-ray radiation dose. This film indicated that the region outside the irradiation zone (bottom-right corner of the 5 ×5 gird)

would receive much less irradiation in all treatments, demonstrating its ability to forecast topographic dose profiles. Gafchromic films function similarly under 1–10 Gy irradiation, but cannot predict 0–0.1 Gy and 10–20 Gy doses (Fig. 4b). When irradiated with 0.06 Gy, 10 Gy, or 20 Gy X-ray, nanoparticle films showed greater signal-to-background ratios (SBR) than the Gafchromic film (Fig. 4c).

Next, we used the nanoparticle film to measure the X-ray dosage in rabbits undergoing 2 cm × 5 cm tumor radiotherapy. The film was covered with a lead plate with a 2 cm × 5 cm oval hole before X-ray irradiation (Fig. S10 online). The nanoparticle film predicted the administered dose with great sensitivity and topographic dose patterns. Moreover, nanoparticle films had higher SBR for predicting low (0.1 Gy) and high (20 Gy) doses than the Gafchromic film.

Clinical dose verification in tumor radiotherapy

We next retrospectively used the nanoparticle film in clinical tumor radiotherapy for topographic dose verification. According to clinical radiotherapy plans, the films received fractionated doses at 0.17–9 Gy for four different malignancies (patient 1, eye tumor, 0.83–5 Gy; patient 2, right lung tumor, 0.17–2 Gy; patient 3, brain tumor, 0.33–3.5 Gy; patient 4, left lung tumor, 1.67–9 Gy) (Fig. S11 online).

Compared with Gafchromic film, the nanoparticle film exhibited more visible color changes and a more similar pattern to therapy planning patterns in four patients (Figs. 5a and S11 online). Then, 4 patients' doses were analyzed using a random 8 × 8 grid. For patient 1, the nanoparticle film predicted ∼ 4.7 Gy in the core irradiation zone (average of the left two vertical columns of the grid), consistent with the treatment plan (4.7 Gy). In contrast, Gafchromic film predicted ∼4.5 Gy (Fig. 5b). In addition, the nanoparticle film predicted that regions near the irradiated regions (3rd to 5th column of the grid, from left to right) received an average dose of 2.8 Gy, which was comparable with treatment planning (2.9 Gy), while Gafchromic film predicted 3.4 Gy. This nanoparticle film also predicted negligible radiation outside the irradiation region (∼ 0.2 Gy), similar to the Gafchromic film. According to therapy planning, dose deviations estimated from the Gafchromic film (average 15%) were 2–7 times greater than those from the nanoparticle film (average 3%) (Fig. S12 online). Similar results were also found in the other three patient dose verifications (Figs. 5b and S12 online).

Next, the radiotherapy effect was evaluated based on the verified X-ray dosages according to the two films in 4T1 tumor cells, Raw 264.7 cells, and bEnd3 cells. Compared with planning-mediated radiotherapy, nanoparticle film-verified radiotherapy had a similar cytotoxic effect on both normal and malignant cells at high X-ray doses (6 or 8 Gy, Fig. 6a-c). In contrast, Gafchromic film-verified radiotherapy at high doses (6 or 8 Gy) resulted in greater death of 4T1 tumor cells, but also greater death of normal cells. Moreover, the calcein-AM/propidium iodide staining further confirmed that the Gafchromic film-verified radiotherapy group had more dead cells (red signals, Fig. 6d and e).

Conclusions

We have reported a high-sensitivity dosimetry technique for retrospective clinical dose verification of patients' radiotherapy plans. In this study, a series of persistent luminescent films based on lanthanide-doped nanoparticles were optimized by varying the nanoparticle concentration and spin-coating speed. The nanoparticle film emitted uniform persistent luminescence after X-ray irradiation, enabling a quantitative reporter for ionizing radiation. This luminescence intensity-based reporter gives the film great detection sensitivity, unlike common X-ray dosimeters that use absorbance as the reporter.

The nanoparticle film showed a greater detection range and sensitivity towards X-ray dose prediction than commercial Gafchromic films. The nanoparticle film accurately measured the administered X-ray dose in both small tumor irradiation in mice and large tumor radiotherapy in rabbits, especially at low (< 0.1 Gy) and high X-ray (> 10 Gy) dosages. For clinical tumor radiotherapy, the nanoparticle film demonstrated high accuracy and sensitivity in visualizing and verifying topographical dose distribution. Moreover, the film is straightforward to make, reusable, inexpensive, and stable. The ability to verify complex clinical X-ray dose distributions by topographic persistent luminescence dosimetry provides a powerful tool to improve the accuracy and precision of radiotherapy and cancer treatment outcome.

CRediT authorship contribution statement

Zichao Luo, Yayun Wu, and Hairong Zheng conceived and designed the project. Xiaogang Liu, Hairong Zheng, and Zonghai Sheng supervised the project and led the collaboration. Zichao Luo and Yayun Wu performed the experiments. Dehong Hu, Duyang Gao, and Yongshuai Ge helped with the experiments. Yuenan Wang contributed to clinical X-ray imaging. Zichao Luo, Yayun Wu, Zonghai Sheng, and Xiaogang Liu analyzed the data. Zichao Luo and Hairong Zheng wrote the paper.

Data availability

Data will be made available on request.

Declaration of Competing Interest

The authors declare that they have no known competing financial interests or personal relationships that could have appeared to influence the work reported in this paper.

Acknowledgments

Appendix A. Supporting information

Supplementary data associated with this article can be found in the online version at doi:10.1016/j.nantod.2023.101854.

References

[1] D. De Ruysscher, G. Niedermann, N.G. Burnet, S. Siva, A.W.M. Lee, F. Hegi-Johnson, Nat. Rev. Dis. Prim. 5 (2019) 1–20.
[2] M. Durante, J. Debus, J.S. Loeffler, Nat. Rev. Phys. 3 (2021) 777–790.
[3] J. Thariat, J.M. Hannoun-Levi, A.S. Myint, T. Vuong, J.P. Gérard, Nat. Rev. Clin. Oncol. 10 (2013) 52–60.
[4] D. Schaue, W.H. McBride, Nat. Rev. Clin. Oncol. 12 (2015) 527–540.
[5] S.M. Bentzen, Nat. Rev. Cancer 6 (2006) 702–713.
[6] E.J. Moding, M.B. Kastan, D.G. Kirsch, Nat. Rev. Drug Discov. 12 (2013) 526–542.
[7] E. Huynh, A. Hosny, C. Guthier, D.S. Bitterman, S.F. Petit, D.A. Haas-Kogan, B. Kann, H.J.W.L. Aerts, R.H. Mak, Nat. Rev. Clin. Oncol. 17 (2020) 771–781.

[8] V.E. Kouloulias, Eur. J. Cancer 39 (2003) 415–422.
[9] A. Adam, L.M. Kenny, Nat. Rev. Clin. Oncol. 12 (2015) 105–113.
[10] P. Andreo, D.T. Burns, A.E. Nahum, J. Seuntjens, F.H. Attix, Fundamentals of Ionizing Radiation Dosimetry, 2nd edition., John Wiley & Sons,, 2017.
[11] P. Olko, Radiat. Meas. 45 (2010) 506–511.
[12] K. Pushpavanam, S. Inamdar, J. Chang, T. Bista, S. Sapareto, K. Rege, Adv. Funct. Mater. 27 (2017) 1606724.
[13] S.N. Ahmed, Physics and Engineering of Radiation Detection, Academic Press,, 2007.
[14] K. Pushpavanam, S. Inamdar, S. Dutta, T. Bista, T. Sokolowski, E. Boshoven, S. Sapareto, K. Rege, Sci. Adv. 5 (2019) eaaw8704.
[15] S. Devic, N. Tomic, D. Lewis, Phys. Med. 32 (2016) 541–556.
[16] S. Devic, Phys Med, 27 (2011) 122–134.
[17] R. Dreindl, D. Georg, M. Stock, Z. Med. Phys. 24 (2014) 153–163.
[18] K. Pushpavanam, E. Narayanan, K. Rege, ChemNanoMat 2 (2016) 385–395.
[19] Y. Tao, M. Li, X. Liu, K.W. Leong, J. Gautier, S. Zha, ACS Appl. Mater. Interfaces 12 (2020) 22499–22506.
[20] A. Jirasek, M. Hilts, K.B. McAuley, Phys. Med. Biol. 55 (2010) 5269–5281.
[21] S. Malekie, F. Ziaie, Nucl. Instrum. Methods Phys. Res. A 791 (2015) 1–5.
[22] H. Liu, H. Qin, N. Shen, S. Yan, Y. Wang, X. Yin, X. Chen, C. Zhang, X. Dai, R. Zhou, X. Ouyang, Z. Chai, S. Wang, Angew. Chem. Int. Ed. 132 (2020) 15321–15326.
[23] J. Wang, P. Mulligan, L. Brillson, L.R. Cao, Appl. Phys. Rev. 2 (2015) 031102.
[24] H. Wei, Y. Fang, P. Mulligan, W. Chuirazzi, H. Fang, C. Wang, B.R. Ecker, Y. Gao, M. Antonietta Loi, L. Cao, J. Huang, Nat. Photonics 10 (2016) 333–339.
[25] W. Pan, H. Wu, J. Luo, Z. Deng, C. Ge, C. Chen, X. Jiang, W. Yin, G. Niu, L. Zhu, L. Yin, Y. Zhou, Q. Xie, X. Ke, M. Sui, J. Tang, Nat. Photonics 11 (2017) 726–732.
[26] Y. Dong, Y. Zou, J. Song, X. Song, H. Zeng, J. Mater. Chem. C 5 (2017) 11369–11394.
[27] E.G. Yukihara, S.W.S. McKeever, C.E. Andersen, A.J.J. Bos, I.K. Bailiff, E.M. Yoshimura, G.O. Sawakuchi, L. Bossin, J.B. Christensen, Nat. Rev. Methods Prim. 2 (2022) 26.
[28] C.A. Mills, H. Al-Otaibi, A. Intaniwet, M. Shkunov, S. Pani, J.L. Keddie, P.J. Sellin, J. Phys. D: Appl. Phys. 46 (2013) 275102.
[29] L. Basiricò, A. Ciavatti, T. Cramer, P. Cosseddu, A. Bonfiglio, B. Fraboni, Nat. Commun. 7 (2016) 1–9.
[30] I. Temiño, L. Basiricò, I. Fratelli, A. Tamayo, A. Ciavatti, M. Mas-Torrent, B. Fraboni, Nat. Commun. 11 (2020) 1–10.
[31] L. Liang, J. Chen, K. Shao, X. Qin, Z. Pan, X. Liu, Nat. Mater. 22 (2023) 289–304.
[32] C. Liu, G. Che, Z. Xu, Q. Wang, J. Alloys Compd. 474 (2009) 250–253.
[33] C.-Y. Tsai, J.-W. Lin, Y.-P. Huang, Y.-C. Huang, Sci. World J. (2014) 102524.
[34] T. Santos, T. Ventura, M.D. Lopes, Radiat. Phys. Chem. 179 (2021) 109217.
[35] X. Ou, X. Qin, B. Huang, J. Zan, Q. Wu, Z. Hong, L. Xie, H. Bian, Z. Yi, X. Chen, Y. Wu, X. Song, J. Li, Q. Chen, H. Yang, X. Liu, Nature 590 (2021) 410–415.
[36] E.Y.L. Marroquin, J.A.H. Gonzalez, M.A.C. Lopez, J.E.V. Barajas, O.A. García-Garduño, J. Appl. Clin. Med. Phys. 17 (2016) 466–481.